

# Flexibility of bacterial flagella in external shear results in complex swimming trajectories

M. Tournus<sup>1</sup>, A. Kirshtein<sup>1</sup>, L. V. Berlyand<sup>1</sup>, and I. S. Aranson<sup>2</sup>

<sup>1</sup>Department of Mathematics, Pennsylvania State University, University Park, Pennsylvania 16802, USA

<sup>2</sup>Materials Science Division, Argonne National Laboratory, 9700 S.Cass Avenue, Argonne, IL 60439, USA  
Engineering Sciences and Applied Mathematics, Northwestern University, 2145 Sheridan Road, Evanston, IL 60202

Email : tournus.magali@gmail.com

## Abstract

Many bacteria use rotating helical flagella in swimming motility. In search for food or migration towards a new habitat, bacteria occasionally unbundle their flagellar filaments and tumble, leading to an abrupt change in direction. Flexible flagella can also be easily deformed by external shear flow, leading to complex bacterial trajectories. Here we examine the effects of flagella flexibility on the navigation of bacteria in two fundamental shear flows: planar shear and Poiseuille flow realized in long channels. On the basis of slender body elastodynamics and numerical analysis, we discovered a variety of nontrivial effects stemming from the interplay of self-propulsion, elasticity, and shear-induced flagellar bending. We show that in planar shear flow the bacteria execute periodic motion, while in Poiseuille flow they migrate towards the center of the channel or converge toward a limit cycle. We also find that even a small amount of random reorientation can induce a strong response of bacteria leading to the overall non-periodic trajectories. Our findings exemplify the sensitive role of flagellar flexibility and shed new light on the navigation of bacteria in complex shear flows.

## 1 Introduction

Bacteria are among the oldest and simplest living organisms on Earth. Bacterial activity influences the planets environmental dynamics in multiple ways, from maintaining soil structure to controlling the biochemistry and photosynthetic productivity of the oceans [1]. To search for food or populate new territories, bacteria often migrate en mass over large distances. This collective behavior is known as swarming motility. Besides many obvious evolutionary advantages, collective behavior appears to be also an effective strategy to prevail against antibiotics [2].

The flow produced in dense bacterial colonies in the course of swarming can be very complex because of the interaction between the bacteria and the fluid [3, 4, 5, 6, 7]. While the flow might visually resemble the turbulent mo-

tion emerging in rapidly stirred fluids, there is a fundamental difference: in hydrodynamic turbulence the mechanical energy is injected at the macroscopic scale, e.g., by stirring the liquid. In contrast, in “bacterial turbulence”, the energy is injected at the microscopic scale by the rotation of helical bacterial flagella, which makes its physical properties deeply distinguished from the turbulent flow of liquid. In particular, the scale of large vortices generated by the collective bacterial locomotion does not depend on the energy injection rate [5, 6]. This complex phenomena, arising due to the intricate interplay between fluid motion and bacterial motility, are difficult to characterize experimentally. Despite significant recent progress in modeling of bacterial collective behavior [8, 9, 10, 11], a predictive model that describes multiple aspects of bacterial turbulence (see for example [12]) has not emerged to date.

Many bacteria use rotating helical flagella for motility and for periodic reorientation, e.g., in response to chemical gradients (chemotaxis) [13]. Peritrichously-flagellated bacteria, such as common *B subtilis* or *E coli* have multiple flagellar filaments distributed over its entire bacterial body. In the course of swimming the filament bundles are spun together. However, bacteria unbundle the filaments and tumble, leading to abrupt reorientation. The transition between the two phases (coiled and unbundle) is triggered by the reversal of a driving motor torque[14]. The flagellar filaments are typically at least twice longer than the bacterial body, and are very flexible, suggesting that they can be easily deformed either by the external shear flow or by the flows of other bacteria. In combination with self-propulsion, the bending of flagella could result in a significant effect on bacterial rheotaxis, i.e. a propensity of microorganism to turn into an oncoming current. It was shown, e.g., that uni-flagellated bacteria exploit flagella buckling to change direction [15, 16]. In addition, flagellum flexibility possibly affects the rheotactic behavior of sperm cells [17, 18, 19].

Recently, the trajectories of self-propelled ellipsoidal rigid swimmers in a 2D Poiseuille flow have been explored. Since the proximity of the boundary can significantly affect bacterial rheotaxis [20, 21], the swimmer is assumed to stay far enough from the walls to exclude those interac-

tions. The propulsion force enables the swimmer to move across the streamlines. The main result is that a self-propelled swimmer in a two-dimensional channel exhibits periodic stable oscillations around the centerline [22, 23]. These periodic trajectories are strongly influenced by random reorientations (tumbling) [24] and the proximity of rigid walls [25, 26]. Bacterial transport appears to be suppressed in shear Poiseuille flow, leading to the depletion of swimmers at the center of the channel [27]. However, the response of bacterial flagella to an applied shear remains poorly understood.

A variety of specific models for helical flagellum have been derived and studied numerically. The pioneering work in that direction is due to [28], who derived from first principles the flow around a moving helix, calculated the associated force and torque, and determined thereby the motion of the helix attached to a large body. In order to understand the propulsion, [29] examined the linear relationships between forces and torques and between translational and angular velocities of helical objects. Specific models were developed for microswimmers. For example, the rotational dynamics of a superhelix towed in a Stokes fluid was studied in [30], and a recent review can be found in [31].

It is also important to distinguish between different mechanisms leading to the alignment and reorientation of microswimmers. Some are due to biological mechanisms, such as chemotaxis [13], whereas others originate due to pure hydrodynamic effects, as a combined effect of the surrounding fluid flow and the specific shape of the body considered. Here we focus on the latter mechanisms. There is also a significant body of works dealing with the response of microswimmers to an external shear flow (rheotaxis), we will mention just a few for review. The study was pioneered in Ref. [17] which pointed out that spermatozoa tend to align in the flow direction, and that this phenomenon is purely due to passive hydrodynamic effects. In [32] the gyrotaxis effect in biflagellated swimming algae was described. Ref. [33] demonstrated that the differences in drag forces between body and flagella lead to preferential alignment with the flow. Recent experiments suggest that rheotaxis may significantly affect the navigation of mammalian sperm cells [18, 19]. The nontrivial rheotactic response of *B. subtilis* bacteria due to chirality of flagella was predicted in [31].

Here, in order to examine the complex response of bacteria in an external shear, we model the swimmer as a flexible entity consisting of a rigid ellipsoidal body attached to a flexible flagellum. The trajectory of the swimmer is represented by the center of mass of the body. To simplify the analysis and exclude side wall effects, we consider bacteria swimming in wide channels. Using elastic slender body dynamics in Stokes flow, we have shown that bacteria can exhibit complex trajectories due to the combined effects of flagellar flexibility and self-propulsion. This behavior is fundamentally different from that predicted for passive ellipsoidal particles [34] that move along streamlines and whose orientation is described by Jeffery orbits [22]. We have examined the behavior of bacteria in two external

shear flows: planar shear between two flat walls moving in opposite directions and two-dimensional Poiseuille flow realized in long flat channels. We have shown that in the case of planar shear flow the bacteria execute periodic orbits, with both the period and the amplitude determined by the shear rate, the shape of the swimmer, and the flexibility of the flagella. For the case of Poiseuille flow we have found that for a realistic range of the parameter values, the swimmer migrates towards the centerline of the channel and swims against the flow. Moreover, for softer flagella, our analysis indicates a different trend: the swimmer executes a periodic motion – a limit cycle. The amplitude of the oscillations around the centerline depends on the flexibility of the flagellum. We have also found that the occasional tumbling of bacteria may have a profound effect on the bacterial swimming trajectories due to the complex interplay between flagellar flexibility and self-propulsion. In particular, we have found that tumbling can result in long non-periodic excursions of the bacteria, mediated by periods of steady swimming along the centerline.

Throughout this paper, we will highlight the difference passive ellipsoid particles [34], active fixed shape ellipsoidal swimmers [22], flagellated non-motile objects (e.g., dead bacteria), and flagellated self-propelled swimmers.

## 2 Model

### Physical framework

Our main hypothesis is that, via its nontrivial coupling between the body orientation and self-propulsion, a flexible flagellum can significantly affect bacterial swimming trajectories and possibly the rheological property of the suspension [36, 37, 38]. We consider a microswimmer in a viscous fluid constituted of an ellipsoidal body linked to a flexible thin rod (flagellum) to explore its behavior in a Poiseuille flow and planar shear flow. For the sake of simplicity we replace the helicoidal flagellum by a thin rod. Also, we neglect effects associated with the counter-rotation of the bacterial body [35]. The self-propulsion is implemented via a tangential force density (traction) distributed uniformly along the rod.

In our model, the geometrical and physical properties we take into account are the length of the flagellum, its propulsion-force and its elasticity.

The bacterial body on a local shear flow undergoes a rotation described by the classical Jeffery equations [34], and is rigidly attached to a flagellum of length  $L$  (see Figure 1). We derive the equation of motion of the flagellum in the framework of slender body theory in the Stokes flow approximation [39]. A somewhat similar derivation is performed in [40] for a free one-armed-swimmer modeled as a slender elastica (not attached to another body), which deforms under the effect of external magnetic torques in a Stokes flow. The novelty of our model lies in the interplay between the flexibility of the flagellum described by the slender elastica, self-propulsion, and external shear flow.

For simplicity we consider that the attachment of flagella filaments to the bacterial body is rigid<sup>1</sup>. We also assume that the microswimmer does not affect the surrounding fluid. In order to exclude wall effects, we consider swimming in wide channels where hydrodynamic and steric interactions with the walls are negligible.

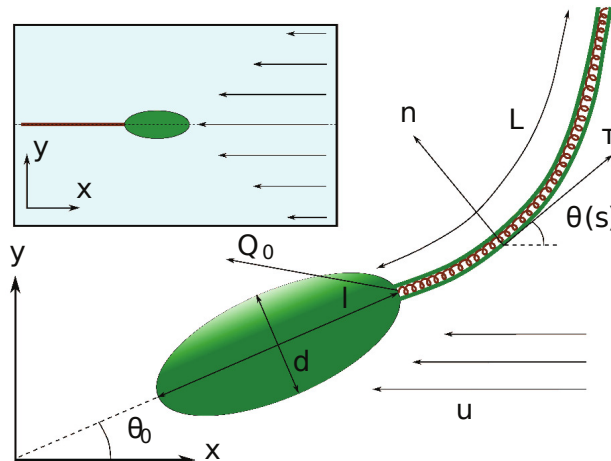


Figure 1: Schematic representation of the swimmer (body + flagellum). Inset: Limiting configuration of the swimmer in Poiseuille flow (on the centerline, resisting the flow).

## Mathematical model

The key ingredient of our model is the classical Jeffery equation (for the body) modified by an additional torque term (coming from the flagellum). This term is determined via coupling the Jeffery's orbits with a corresponding nonlinear 4th order equation for the flagellum derived from basic physical principles. The flow is assumed to be parallel to the  $x$  axis and its velocity vector is  $u(y)\mathbf{e}_x$ . Here we summarize the model in dimensionless form (see Methods 6.1).

Since the bacterial body is modeled by a rigid ellipsoid, we describe its motion by a Jeffery equation [34] with parameter  $\beta$ , the Bretherton constant of the body ( $\beta = 0$  for needles and  $1/2$  for spheres), where the shear rate is taken to be the flow rate  $u'(y^h)$  at the center of the ellipsoid ( $y^h$  is the  $y$ -coordinate of the center of mass of the ellipsoid, and the fluid velocity does not depend on  $x$ ). We add an additional term  $N_0$  corresponding to the normal internal stress due to the flagellum. The modified Jeffery equation is written as

<sup>1</sup>Individual flagellar filament is attached to body via a soft hook. As it was shown in [16], the flexibility and buckling of the hook plays a profound role in the tumbling of uni-flagellated bacteria. However, in the case of bacteria with multiple flagellar filaments distributed over the bacterial body, such as *Bacillus subtilis*, flexibility due to soft hook coupling is not important since the flagella form tight bundles.

$$\begin{cases} \frac{d\theta_0}{dt} = -u'(y^h) \left( (1 - \beta) \sin^2 \theta_0 + \beta \cos^2 \theta_0 \right) + \frac{3L}{l} k_r N_0, \\ \theta_0(0) = \theta_{0,in}, \end{cases} \quad (1)$$

where  $\theta_0$  is the orientation of the swimmer body (see Figure 1),  $l$  and  $L$  are respectively the length of the body and of the flagellum, and  $k_r$  is a ratio between the drag coefficients of the body and flagellum (end of Section 6.1).

The flagellum is represented by a 1D elastica of bending rigidity  $K_b$  parametrized by the non-dimensional arclength  $0 \leq s \leq 1$ . We denote by  $\theta(s, t)$  the angle between the flagellum and the  $x$ -axis (see Figure 1). We denote by  $\mathbf{Q}$  the integrated internal stress in the flagellum and by  $\mathbf{Q}_0$  the force exerted by the flagellum on the body decomposed on the Frenet basis  $(\boldsymbol{\tau}, \mathbf{n})$  of the flagellum as

$$\mathbf{Q} = \Lambda \boldsymbol{\tau} + N \mathbf{n}, \quad \mathbf{Q}_0 = \Lambda_0 \boldsymbol{\tau} + N_0 \mathbf{n}. \quad (2)$$

The equations describing the shape and motion of the flagellum are derived from the balances of forces and internal torques (see Methods, equations (20) and (22)). The forces taken into account are the fluid friction force (proportional to the relative velocity between the flagellum and the fluid according to resistive force theory) and the propulsion force, generated by an internal motor. The force density  $F_p$  is assumed constant along the flagellum. Typical value for the total force is about 1 pN, and length of the flagellum is about 10  $\mu\text{m}$ , so the density force is of 0.1  $\mu\text{N}/\text{m}$ . The balance of forces provides a vectorial relation decomposed on the Frenet basis. Substituting balance equations into geometrical identities (see Methods, equations (27)) we obtain two scalar equations for the angle  $\theta$  and stress  $\Lambda$

$$\begin{aligned} \frac{\partial^2 \Lambda}{\partial s^2} &= \frac{1}{\alpha} \Lambda \left( \frac{\partial \theta}{\partial s} \right)^2 - K_b \left( \frac{\partial^2 \theta}{\partial s^2} \right)^2 - \frac{u'(y)}{2} \sin(2\theta) \\ &\quad - \frac{(\alpha + 1)}{\alpha} K_b \frac{\partial^3 \theta}{\partial s^3} \frac{\partial \theta}{\partial s}, \quad t \geq 0, \end{aligned} \quad (3)$$

and

$$\begin{aligned} \frac{\partial \theta}{\partial t} &= -\frac{K_b}{\alpha} \frac{\partial^4 \theta}{\partial s^4} + \left( \frac{1}{\alpha} \Lambda + K_b \left( \frac{\partial \theta}{\partial s} \right)^2 \right) \frac{\partial^2 \theta}{\partial s^2} \\ &\quad + \left( \frac{\alpha + 1}{\alpha} \frac{\partial \Lambda}{\partial s} + F_p \right) \frac{\partial \theta}{\partial s} - u'(y) (\sin^2(\theta)), \quad (4) \\ t > 0, \quad \theta(s, 0) &= \theta_{in}(s) \end{aligned}$$

where  $\alpha$  is a drag anisotropy factor taking into account the shape of the flagellum.

The physical hypotheses included in equations (3) and (4) are the inextensibility and the elasticity of the flagellum (see Methods, equations (21) and (26)).

Equations (3) and (4) come with a set of boundary conditions, encoding the fact that the end of the flagellum is free at  $s = 1$ ,

$$\frac{\partial \theta}{\partial s}(1, t) = \frac{\partial^2 \theta}{\partial s^2}(1, t) = \Lambda(1, t) = 0, \quad (5)$$

and the interface between the body and the flagellum is rigid

$$\theta(0, t) = \theta_0(t), \quad \Lambda(0, t) = \Lambda_0(t), \quad (6)$$

The balance of internal torques combined with rigid attachment between the body and the flagellum provides the expression of  $N_0$

$$N_0(t) = -K_b \frac{\partial^2 \theta}{\partial s^2}(0, t). \quad (7)$$

Another consequence of rigid attachment is the equality of the velocity at the interface body/flagellum. This vectorial equality provides directly two scalar equations, corresponding to the tangential part

$$k_r \Lambda_0 = \frac{\alpha}{L} \left( u(y(0)) - u(y^h) \right) \cos(\theta_0) + \frac{\partial \Lambda}{\partial s} + F_p - \frac{\partial \theta}{\partial s} N_0, \quad (8)$$

and to the normal part of the velocity equality.

$$\begin{aligned} \left( \frac{\alpha}{\alpha_h} + \frac{3\alpha}{2} \right) k_r N_0 &= -\frac{\alpha}{L} \sin(\theta_0) \left( u(y(0)) - u(y^h) \right) \\ &+ \frac{\alpha l}{2L} u'(y) \left[ (1 - \beta) \sin^2(\theta_0) + \beta \cos^2(\theta_0) \right] \\ &+ \left[ -K_b \frac{\partial^3 \theta}{\partial s^3} + \frac{\partial \theta}{\partial s} \Lambda \right], \end{aligned} \quad (9)$$

These two last algebraic equations only hold at  $s = 0$ .

To close the system, since the fluid velocity and thus the shear rate ( $u'(y)$ ) may depend on swimmer coordinate  $y$ , we need to localize the swimmer. The  $y$ -coordinate of the body satisfies the following ordinary differential equation, similarly to [23]

$$\begin{cases} \frac{dy^h(t)}{dt} = k_r \Lambda_0(t) \sin(\theta_0(t)) + \frac{k_r}{\alpha_h} N_0(t) \cos(\theta_0(t)), \\ y^h(0) = y_0^h. \end{cases} \quad (10)$$

and the position along the flagellum follows from geometrical considerations

$$\begin{cases} \frac{\partial y(s, t)}{\partial s} = \sin(\theta(s, t)), \\ y(0, t) = y^h(t) + \frac{l}{2L} \sin(\theta_0(t)). \end{cases} \quad (11)$$

The  $x$ -coordinates are not needed, however, their expression is provided in the Methods section, since they are used to plot the trajectories.

### 3 Results

In this section, the model is studied numerically for two types of shear flows: a planar shear (linear profile) and a Poiseuille flow (nonlinear profile). The equations for the flagellum, (3) and (4), are solved using a centered finite difference scheme on a uniform grid ( $\sim 100$  point per micron on the flagellum and  $10^{-2}$ s timestep). In (4), the fourth and second order derivatives are taken implicitly, which still allows for the resolution of the scheme without

iterations. We compute  $N_0$  from the boundary condition and substitute its value into (1), which we solve with the forward Euler scheme. The numerical scheme is implemented in C++. See Supplementary Material S2.

#### 3.1 Planar shear flow

In a planar shear flow, we compare the outcome of the numerical study to a theoretical result derived in the asymptotic limit of large bending stiffness  $K_b \gg 1$  of the (rigid) flagellum. The fluid speed in planar shear flow is given by

$$u(y) = \gamma y. \quad (12)$$

We observe periodic trajectories (see Figure 2). When starting close to the centerline, the trajectory is closed (see Figure 2(a)). However, when starting on the upper part of the channel, there is a drift toward the right after one period, because the swimmer spends more time in the upper part of the channel than in the lower part. The value of the drift linearly depends on the  $y$ -initial position and vanishes when starting at  $y = 0$ . (See video in suppl. material). For analysis, we linearize Eqs. (1),(3)-(9) around the state given by  $K_b \rightarrow \infty$ , and perform a multiscale perturbation method.

From (3)-(9), in the limit of large  $K_b$  the evolution of the bacterial body angle is given asymptotically by

$$\theta_0^0(t) = \arctan \left[ \sqrt{\frac{b}{1-b}} \tan \left( t \sqrt{b(1-b)} \left( 1 + \frac{c}{K_b b} \right) \right) \right]. \quad (13)$$

Here  $b$  and  $c$  are geometrical constants, which only depend on  $L, l, \alpha, \alpha_h, k_r$  and  $\beta$  (see Supplementary Material S1).

Equation (13) describes how the period of the body angle  $\theta^0$  depends on the bending stiffness  $K_b$ . For large bending stiffnesses, the body rotates according to the Jeffery equation with parameter  $b < \beta$ . As expected, the effective aspect ratio of the flagellated swimmer is larger than that of the non-flagellated one. The flagellum amplifies the contrast between slow rotation (swimmer parallel to the flow) and fast rotation (swimmer perpendicular to the flow). The relation given by Eq. (13) as well as the corresponding numerical solution are plotted in Figure 2(b), using the values established in the literature for *B. Subtilis*. The result shows that the period of the body rotation decreases when the flagellum becomes softer (smaller bending stiffness). As expected, in the limit of large  $K_b$  there is a good agreement between the asymptotic analysis and numerics.

The decrease of the rotation period with the decrease in bending stiffness can be understood as follows. A softer flagellum on the average bends more than a rigid one. As a result, a swimmer with a bent flagellum has an effectively smaller aspect ratio than with a more rigid one. In turn, the rotation period decreases with the increase in aspect ratio.

Thus, in a planar shear flow, as for non-flagellated swimmers [34], the trajectories of flagellated swimmers are periodic, and the period is mainly determined by the

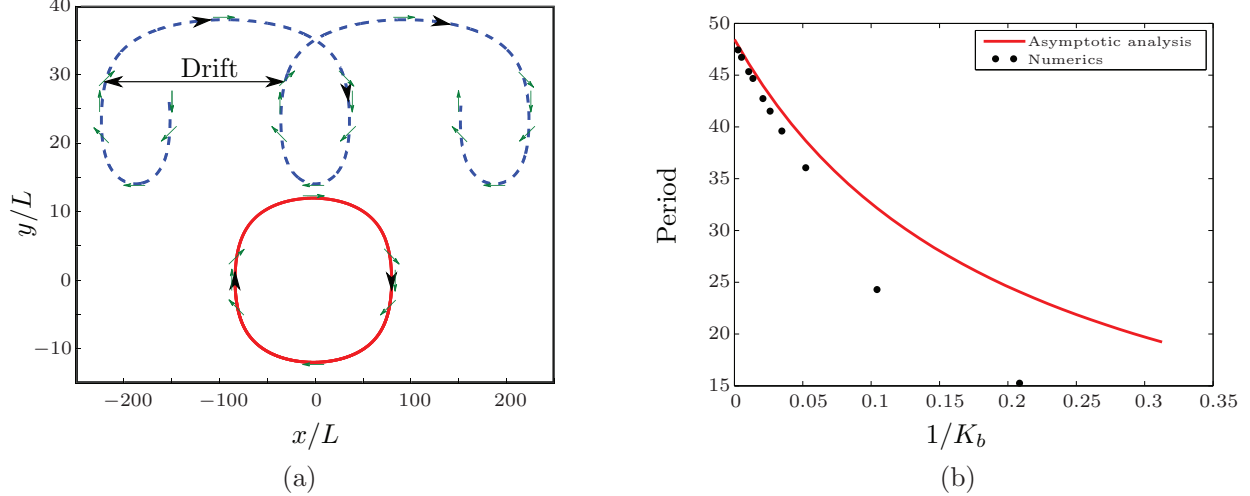


Figure 2: (a): Trajectories of the self-propelled swimmer in a planar shear flow for two different initial positions. Green arrows indicate the orientation  $\theta_0(t)$  of the swimmer body. (b): Dependence of the rotation period on  $\frac{1}{K_b}$ , where  $K_b$  is the bending stiffness (dimensionless, see Methods 6.1, rescaling) The red line is the period extracted by formula (13). The dots are corresponding numerical results. Other parameters are taken as written in Table 1. For comparison, the rotation period of similar non-flagellated swimmer is about 23 s.

elasticity of the flagellum: the softer the flagellum, the smaller the period.

Dependence of the period on the length of the flagellum can be thought as a competition of two effects. On one hand, longer flagellum increases effective aspect ratio of the flagellated swimmer. On the other hand, the longer the flagellum is, the easier it is to bend. Numerical results show that the period has local maximum when  $L \approx 9 \cdot 10^{-6}$  (with other parameters as written in Table 1).

Let us point out that the shape of the flagellum strongly depends on  $K_b$  and that a buckling instability occurs up to a threshold which is about a hundred times smaller than the realistic value  $K_b = 3 \times 10^{-23}$ . (see the electronic Supplementary Material S2).

### 3.2 Poiseuille flow

The majority of experiments [19, 20, 27] are performed in a rectangular channel of width  $w$  (or in circular channel of radius  $r_0$ ). In the planar geometry, assuming no-slip boundary conditions, the  $x$ -component of fluid velocity has the following parabolic profile,

$$u(y) = p \left( y^2 - \frac{w^2}{4} \right), \quad (14)$$

where  $p$  is the applied pressure normalized on the dynamic viscosity of suspending liquid.

First, we demonstrate the stability of steady-state swimming along the centerline. In [23], the trajectories of a self-propelled ellipsoidal swimmer (with point-force propulsion) in a Poiseuille flow are shown to be periodic. The presence of the flagellum makes our system more difficult to deal with, nevertheless, in the large  $K_b$  limit the

properties of the trajectories can be studied analytically. In particular, it is clear that the states  $[y = 0, \theta = 0]$  and  $[y = 0, \theta = \pi]$  (i.e. the swimmer with a straight flagellum swims along the centerline) are the only stationary states of the system. In the large  $K_b$  limit, the state  $[y = 0, \theta = \pi]$  (i.e. swimming against the flow) is the only linearly stable equilibrium.

The linearized system around the stationary state  $[y = 0, \theta = \pi]$  is of the form:

$$\begin{cases} \frac{d\theta_0(t)}{dt} = -2py(t) + 3N_0(t), \\ \frac{dy(t)}{dt} = \frac{F_p \cos(\pi)}{3} \theta_0(t) + \frac{\cos(\pi)}{4} N_0(t), \end{cases} \quad (15)$$

where  $N_0$  is determined by

$$\begin{cases} \frac{\partial \theta}{\partial t}(s, t) = -\frac{K_b}{2} \frac{\partial^4 \theta}{\partial s^4} + \frac{F_p}{3} (1-s) \frac{\partial^2 \theta}{\partial s^2}, \\ N_0 = -K_b \frac{\partial^2 \theta}{\partial s^2}(s=0) \\ N_0 = -\frac{\beta p}{4} y - \frac{K_b}{2} \frac{\partial^3 \theta}{\partial s^3}(s=0) + \frac{F_p}{3} \frac{\partial \theta}{\partial s}(s=0), \\ \frac{\partial \theta}{\partial s}(1, t) = \frac{\partial^2 \theta}{\partial s^2}(1, t) = 0, \quad \theta(0, t) = \theta_0(t). \end{cases} \quad (16)$$

We recall that  $F_p < 0$ , which implies that the second order term in the first line of (16) causes a buckling instability. If there is no flagellum, i.e.  $N_0 = 0$ , the matrix of the linear system  $\frac{d}{dt} (\theta_0, y)^T = A (\theta_0, y)^T$  is

$$A = \begin{pmatrix} 0 & -2p \\ \frac{F_p \cos(\pi)}{3} & 0 \end{pmatrix}.$$

$Tr(A) = 0$  and  $Det(A) > 0$ , which means that the eigenvalues are imaginary. From (16),  $N_0$  is computed as

$$N_0 = -\frac{1}{3} \left( \frac{d\theta_0}{dt} + \beta p y \right). \quad (17)$$

Substitution of (17) into the linear system (15) gives us, after straightforward computations, that  $[y = 0, \theta = \pi]$  is stable whereas  $[y = 0, \theta = 0]$  is not. This is in agreement with the numerical observation that in Poiseuille flow, for large enough values of the bending stiffness, the bacteria swim opposite to the flow direction for large times. The bacterium was launched at  $y = 5$ , with an angle  $\theta_0 = 0$  (i.e. parallel to the walls) and a straight flagellum. The swimmer performs large loops, first in the upper part of the channel, then in both halves (see Figure 3(a)). The amplitude of the loops is decreasing with time, and at the end, the swimmer converges to the centerline of the channel and orients against the flow (see inset to Figure 1).

The flow strength was taken sufficiently high to avoid any collision between the swimmer and the wall. Thus the swimmer always drifts downstream. Due to the vorticity of the flow, the swimmer first (short time,  $x \approx -10^4$  on Figure 3 (a)) performs a “tumbling” motion (as defined in [22]), i.e. the body is undergoing complete rotation, in one part of the channel and has a slight drift toward the center of the channel<sup>2</sup>. Due to this drift, after some time, the swimmer crosses the centerline. It then begins (at an intermediate time) to visit both sides of the channel, performing a “swinging” motion (as defined in [22]), i.e. the body oscillates around the angle  $\pi$ , because the difference of vorticity between the upper- and lower-side of the channel prevents it from undergoing a complete rotation. However, due to the flagella flexibility, the amplitude of the excursions becomes smaller and smaller, and for large time, the swimmer reaches a stable stationary state, in stark contrast with the behavior of a swimmer modeled by a rigid body without a flagellum. The equations describing the trajectory of a self-propelled fixed shape ellipsoidal swimmers have been studied in [23] where the authors observed two different periodic behaviors, “tumbling” and “swinging”, depending on the  $y$ -coordinate of the initial position. In our case, there is a drift towards the center of the channel due to presence of the flagellum, which breaks the periodicity of the trajectories and allows the swimmer to switch from “tumbling” motion to “swinging” motion (see Figure 3(b), non-closed and closed curves respectively).

### 3.2.1 Heuristics for the convergence toward the centerline for large bending stiffness

Here we present a simple explanation of why the swimmer converges toward the centerline due to its flagellum flexibility in the case where the flagellum is rigid enough.

<sup>2</sup>Here we distinguish “tumbling” motion due to vorticity of the flow from “run-and-tumble” behavior of bacteria due to unbundling of flagella

Two mechanisms are responsible for the convergence toward the center: the elastic response of the flagellum tends to displace the center of mass of the swimmer, and the propulsion force amplifies this phenomenon.

**The propulsion force amplifies the drift toward the center.** First, the convergence toward the center is not a sole property of self-propelled swimmers. Numerical results show that our flagellated object (e.g., dead bacterium) with no propulsion force (i.e for  $F_p = 0$ ) undergoes a slight drift toward the center of the channel (see Figure 3 (d),  $K_b = 3 \cdot 10^{-23}$ ). Under assumptions used in [34] passive ellipsoid is expected to drift along the streamlines. This small drift toward the center is negligible comparing to the lift force that occurs to the nonlinear profile of the Poiseuille flow [42], which in contrast, makes the swimmer migrate away from the center (see Section 6.2.1). However, for self-propelled swimmers, the migration toward the center is amplified by the propulsion force, whereas the lift force is not.

**The elastic response of the flagellum tends to displace the center of mass of the swimmer.** For large enough bending stiffness (e.g., larger than  $3 \cdot 10^{-23}$ ) there is an overall tendency of the flagellum to straighten due to the bending rigidity described by the fourth order term in (4). This phenomenon results in a net displacement of the body, for both self and non-self propelled swimmers, and the direction of the body displacement is the orientation of the body. The  $y$ -component of this displacement determines if the swimmer drifts toward or away from the center. The higher the shear rate experienced by the flagellum, the more important the vertical displacement. Because the shear rate experienced by the flagellum is higher when further from the centerline, this displacement is more important when the swimmer is oriented toward the center.

**Why convergence toward the center does not occur in planar shear flow?** The migration toward the center is not observed in planar shear flow. The reason is the following: In a planar shear flow, whatever the orientation of the swimmer is, the shear experienced by each point of the flagellum only depends on the position of the body (since the shear rate is constant everywhere). No direction (away or toward the center) is privileged.

### 3.2.2 Non-monotone dependence of the limiting behavior on the bending stiffness

The heuristic explanation we provided above is no longer valid for small values of the bending stiffness. For the chosen value of dimensionless pressure gradient  $p = 10^4$  and smaller bending stiffness  $K_b = 10^{-24}$  (representative value for *Bacillus subtilis* is  $K_b = 3 \cdot 10^{-23}$ ) the self-propelled swimmer no longer drifts toward the center, but instead converges towards a limit cycle (see Figure 3(c)), where the swimmer swings around the centerline. When further decreasing the bending stiffness ( $K_b = 2 \cdot 10^{-25}$ ), the behavior is again similar to  $K_b = 3 \cdot 10^{-23}$ . This suggests that the behavior of the system is highly nontrivial.

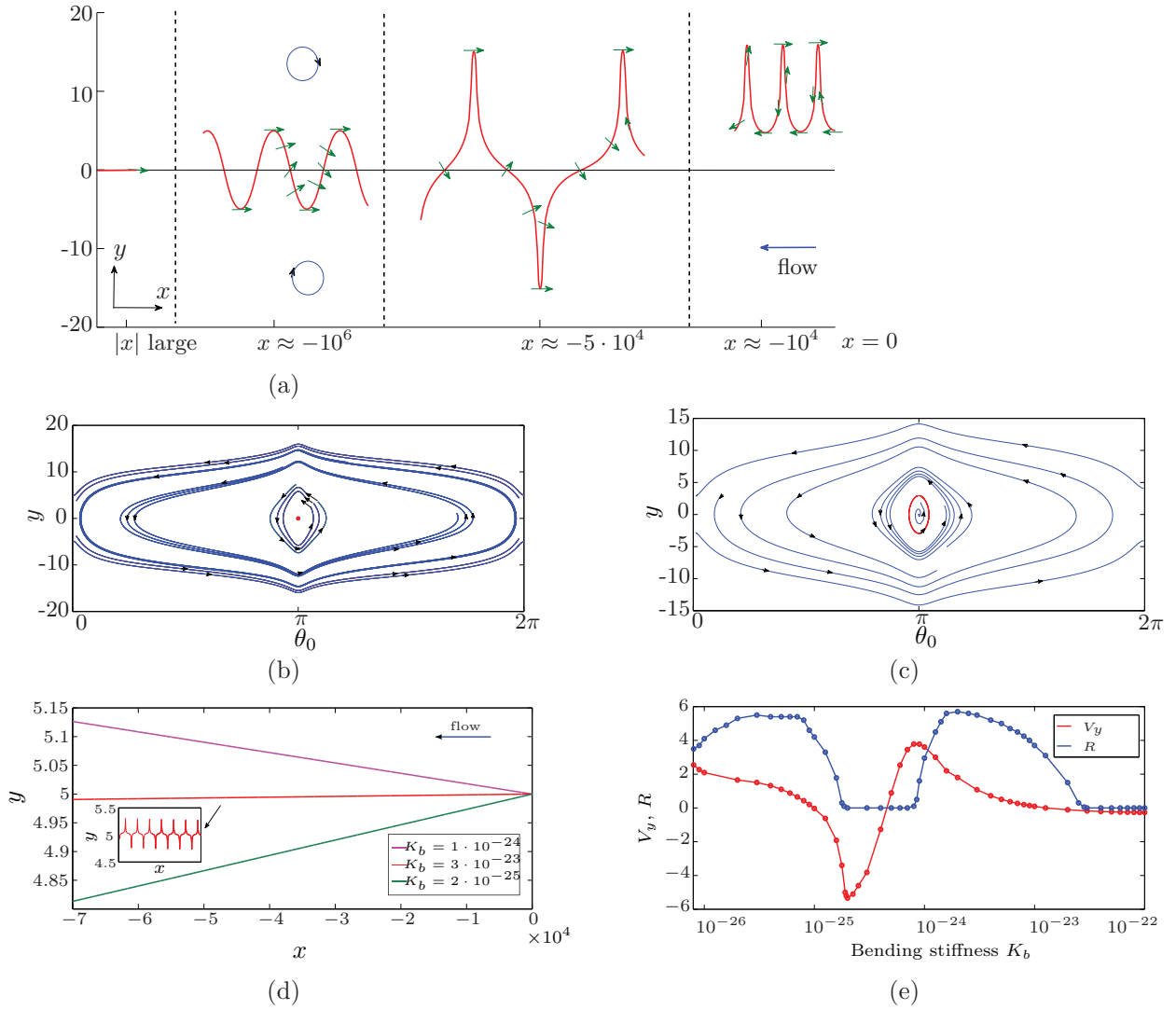


Figure 3: (a): Representative trajectory  $(x(t), y(t))$  of the swimmer in the channel for different intervals of time, for the physical value of the bending stiffness ( $K_b = 3 \cdot 10^{-23}$ ). The arrows indicate the orientation  $\theta_0(t)$  of the swimmer body. The blue circles indicate the sign of the vorticity. (b) and (c): Phase portraits of the trajectories of the self-propelled swimmer. For large values of the bending stiffness, the swimmer converges toward the center of the channel swimming against the flow (b), for a smaller value of the bending stiffness, there is a limit cycle (c). (d): Averaged trajectory over a period of the passive swimmer for three different bending stiffness. Depending of the bending stiffness value, there is an averaged drift toward or away from the center. The inset corresponds to the real shape of the trajectory. The convergence is slow, so we need to consider large values on the  $x$  - axis (downstream). (e): Averaged  $y$  velocity of the passive swimmer  $\langle V_y \rangle$  vs bending stiffness compared to the size of the limit cycle  $R$  vs bending stiffness for the self-propelled swimmer. Dots correspond to values given by the numerical scheme, the dotted lines are an interpolation of the dots.  $R$  is the maximum distance from the center of the channel that the swimmer reaches in large time (i.e  $R := \limsup_{t \rightarrow \infty} |y_0(t)|$ ). Except for  $K_b$ , parameter values were taken as written in Table 1 and  $p = 10^4$  1/m.s. The vertical line indicate the buckling threshold.

It has been observed numerically that depending on the bending stiffness of the flagellum, the non self-propelled flagellated object ( $F_p = 0$ ) can either drift toward the walls or toward the center (see Figure 3(d),  $K_b = 10^{-24}$  and  $K_b = 9 \cdot 10^{-24}$  respectively). Also, we observed the self-propelled swimmer reaching either a stable stationary state, or a limit cycle. For different bending stiffness values the  $y$ -averaged velocity of a non self-propelled object is plotted on Figure 3(e). If the averaged velocity is negative (e.g.  $K_b \geq 3 \cdot 10^{-23}$ ), the non self-propelled object tends to reach the center of the channel. If the averaged velocity is positive (e.g.  $K_b = 10^{-24}$ ), the swimmer migrates away from the center. Clearly, there is a strong correlation between the size of limit cycle  $R$  for self-propelled swimmer and average  $y$  velocity  $\langle V_y \rangle$  of non-motile flagellated body, see Figure 3(e). Ranges of the bending stiffness where the averaged velocity of the non self-propelled object is negative correspond approximately to ranges where the self-propelled swimmer converges toward the center (size of the limit cycle = zero). Conversely, ranges of the bending stiffness where the averaged velocity of the non-motile body is positive correspond to ranges where the self-propelled swimmer converges toward a limit cycle. It means that the bending stiffness value determines the qualitative behavior of the swimmer.

When decreasing  $F_p$ , but staying close to the physical value (50%), the curve  $R$  is slightly shifted on the left and has a smaller amplitude. The pressure gradient of the flow  $p$  on the other hand does not affect qualitatively the large time behavior of the swimmer, but it has a quantitative effect: the ranges of values of  $K_b$  where the swimmer converges toward the stationary state or the limit cycle are the same, whatever  $p$ . However, increasing  $p$  accelerates the convergence toward the steady state, and reduces the size  $R$  of the limit cycle.

### 3.2.3 Random reorientation (tumbling events)

For large values of the bending stiffness, the swimmer asymptotically converges toward the centerline. However, tumbling, that is in that context an abrupt reorientation of a swimmer, may destabilize the steady state. To verify this assumption, we incorporated random reorientation in our model. A good approximation to the probability distribution of tumbling events in time is a Poisson distribution, [41]. It implies that the total number of tumbles occurring between time  $s$  and  $t$  is a Poisson random variable with parameter  $\lambda_r(t - s)$ , where  $\lambda_r$  is the intensity of the Poisson law. The Poisson process determines the instant of reorientation, and the angle changes according to the uniform distribution on  $[0, 2\pi]$ . The flagellum reorients as well with the same angle. With random reorientation present, the relaxation toward the steady state no longer occurs. We display on Figure 4 two selected time intervals at which tumbling occurs. Recall that the fluid is moving in the negative direction, so that each plot has to be read from right to left. On plots (a) and (b), the swimmer undergoes a “swing” when the tumble event occurs. If no

random reorientation, the angle of the body would have relaxed toward  $\pi$  and the  $y$ -amplitude of the trajectory would have decreased to  $y = 0$ . The tumble event reorients the swimmer and makes it switch to another point of the phase portrait Figure 3, panel (b). On Figure 4, panel (a), after the tumble event the swimmer is still “swinging”, but the amplitude of the trajectory has increased. On plots (c) and (d), the swimmer was also undergoing a “swinging” motion when the tumble event occurs. The new orientation of the swimmer is  $3\pi/2$ , and the motion switches to a “tumbling” motion (i.e. the swimmer is undergoing a complete rotation) on the lower part of the channel. Thus, the qualitative behavior of the swimmer may drastically change due to a relatively rare random reorientation, eliminating the overall convergence to the centerline.

## 4 Conclusions

We introduced a non-linear model based on partial differential equations that couples body motion of a swimmer with flexible flagellum attached to it. Linear asymptotic analysis of this model for planar shear flow shows how classical Jeffery orbits change due to the flagellum. In particular, we found the dependence of the body rotation period on the bending stiffness of the flagellum. Next, we performed numerical analysis of this model in Poiseuille flow and made several important observations. First, the model exhibits non-periodic trajectories due to the presence of the flagellum. This stands in contrast with classical periodic trajectories for Jeffery equation for passive particles, and even more striking, when compared to periodic trajectories for fixed shape active swimmers [23] that are self-propelled but have no flagellum. Second, we observe that the large time behavior of our system is non-monotonic with respect to the bending stiffness. Namely, for large bending stiffness, the system reaches a steady state. When bending stiffness is decreased, it converges towards limit cycle. Further decrease in the bending stiffness results in the system reaching the steady state again. Finally, we observe that even a small amount of random tumbling events drastically affect the above described behavior.

## 5 Acknowledgments

The theoretical work was supported by the NIH grant 1R01GM104978-01. The simulations at Argonne and work of I.S.A. were supported by the U.S. DOE BES, Division of Materials Science and Engineering (IA)



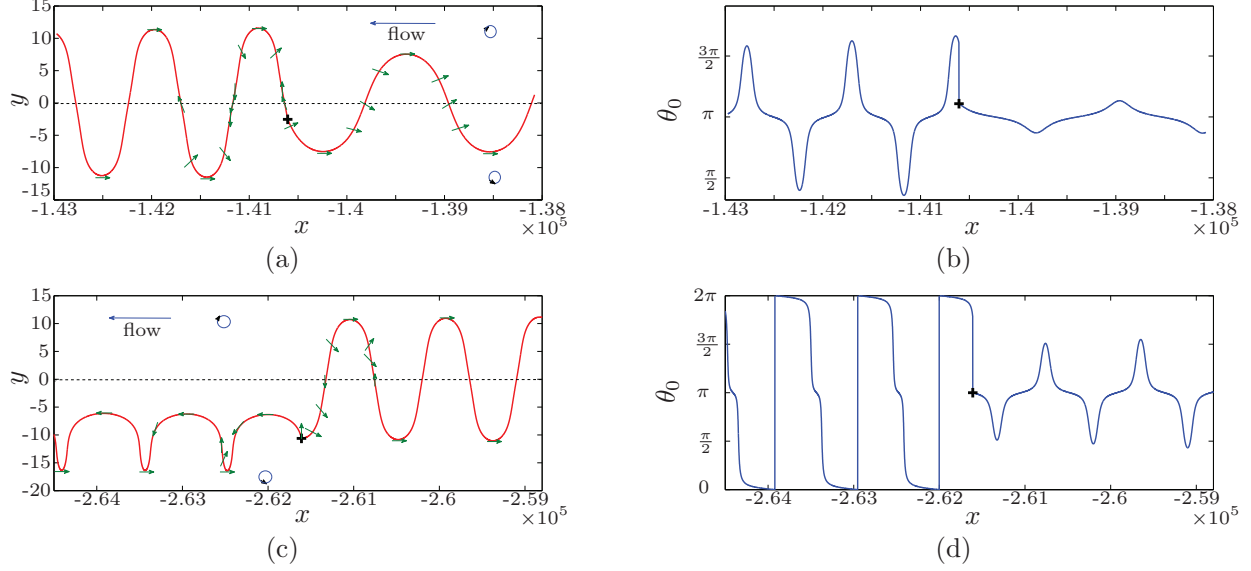


Figure 4: (a) and (c): Trajectories of the self-propelled swimmer in the  $(x, y)$  space for two selected time intervals. The fluid flows from the right to the left and the blue circles indicate the sign of the vorticity. Green arrows indicate the orientation  $\theta_0(t)$  of the swimmer body. The symbol '+' shows the tumbling events. (b) and (d): Orientation  $\theta_0$  of the swimmer as a function of  $x$ . The intensity of the Poisson process is taken to be 0.1/min, which means that a tumbling event occurs in average every 10 minutes. Other parameters are taken as written in Table 1.

## 6 Methods

### 6.1 Derivation of the equations of motion

#### The flexible flagellum

To derive the equations of motion we employ resistive force theory and theory of the elasticity of a slender body. We use the arclength  $0 \leq s \leq L$  to parametrize the flagellum. We denote by  $\theta(s, t)$  the angle between the flagellum and the  $x$ -axis (see Figure 1). We also introduce the local tangent, normal, and binormal vectors,

$$\boldsymbol{\tau} = \begin{pmatrix} \cos(\theta) \\ \sin(\theta) \\ 0 \end{pmatrix}, \quad \mathbf{n} = \begin{pmatrix} -\sin(\theta) \\ \cos(\theta) \\ 0 \end{pmatrix}, \quad \mathbf{b} = \begin{pmatrix} 0 \\ 0 \\ 1 \end{pmatrix},$$

and write the velocity of the point of the flagellum as

$$\mathbf{v} = v_\tau \boldsymbol{\tau} + v_n \mathbf{n}. \quad (18)$$

Denoting by  $\mathbf{Q}$  the integrated internal stress in the flagellum and by  $\mathbf{Q}_0$  the force exerted by the flagellum on the body,

$$\mathbf{Q} = \Lambda \boldsymbol{\tau} + N \mathbf{n}, \quad \mathbf{Q}_0 = \Lambda_0 \boldsymbol{\tau} + N_0 \mathbf{n}. \quad (19)$$

In the framework of the resistive force theory, the force exerted by the fluid on the flagellum is proportional to the relative velocity between the flagellum and the fluid. The force balance states that the divergence of the internal stress is equal to the external force applied to the

flagellum, yielding the following relations

$$\begin{aligned} \frac{\partial}{\partial s} (\Lambda \boldsymbol{\tau} + N \mathbf{n}) &= \zeta_f (v_\tau - u(y) \cos \theta) \boldsymbol{\tau} \\ &+ \alpha \zeta_f (v_n + u(y) \sin \theta) \mathbf{n} - F_p \boldsymbol{\tau}. \end{aligned} \quad (20)$$

Here,  $F_p$  is the propulsion force density generated by the flagellum. The parameter  $\zeta_f$  is the drag coefficient of the flagellum, and  $\alpha$  is a drag anisotropy factor due to the shape of the flagellum. Following [40], we set  $\zeta_f = 2\pi\eta_0/\log(L/D)$ , where  $\eta_0$  is the viscosity of the fluid, and  $\alpha = 2$  (slender body). The elasticity of the flagellum is represented by the constitutive relation

$$\mathbf{M} = K_b \kappa \mathbf{b}, \quad (21)$$

where  $\kappa$  is the local flagellum curvature, defined by  $\kappa = \frac{\partial \theta}{\partial s}$ . The balance of internal torques gives

$$\frac{\partial \mathbf{M}}{\partial s} + \boldsymbol{\tau} \times \mathbf{Q} = 0, \quad (22)$$

which combined with (21) gives an expression of the normal component of the internal stress

$$N = -K_b \frac{\partial^2 \theta}{\partial s^2}. \quad (23)$$

The force balance vector relation (20) can be separated into the tangential and normal parts

$$\begin{aligned} \zeta_f v_\tau &= \zeta_f u(y) \cos \theta + \frac{\partial \Lambda}{\partial s} + F_p - \kappa N, \\ \alpha \zeta_f v_n &= -\alpha \zeta_f u(y) \sin \theta + \frac{\partial N}{\partial s} + \kappa \Lambda. \end{aligned} \quad (24)$$

We derive the equations for  $\Lambda$  and  $\theta$ , using the geometrical Frenet relations

$$\frac{\partial \boldsymbol{\tau}}{\partial s} = \kappa \mathbf{n}, \quad \frac{\partial \mathbf{n}}{\partial s} = -\kappa \boldsymbol{\tau},$$

yielding

$$\frac{d\boldsymbol{\tau}}{ds} = \frac{dv}{ds} = \left( \frac{\partial v_\tau}{\partial s} - \kappa v_n \right) \boldsymbol{\tau} + \left( \frac{\partial v_n}{\partial s} + \kappa v_\tau \right) \mathbf{n}. \quad (25)$$

The inextensibility of the flagellum can be cast in the form

$$\frac{d\boldsymbol{\tau}}{ds} = \left( \frac{\partial \theta}{\partial t} \right) \mathbf{n} \quad (26)$$

By identifying the terms in (25) and (26) we obtain

$$\frac{\partial v_\tau}{\partial s} = \kappa v_n, \quad \frac{\partial \theta}{\partial t} = \frac{\partial v_n}{\partial s} + \kappa v_\tau, \quad (27)$$

which gives us the following equations on  $\Lambda$  and  $\theta$

$$\begin{aligned} \alpha \frac{\partial^2 \Lambda}{\partial s^2} &= \left( \frac{\partial \theta}{\partial s} \right)^2 \Lambda - \alpha K_b \left( \frac{\partial^2 \theta}{\partial s^2} \right)^2 - \frac{\alpha}{2} u'(y) \zeta_f \sin(2\theta) \\ &\quad - \frac{\partial \theta}{\partial s} (\alpha + 1) K_b \frac{\partial^3 \theta}{\partial s^3}, \end{aligned} \quad (28)$$

$$\begin{aligned} \alpha \zeta_f \frac{\partial \theta}{\partial t} &= -K_b \frac{\partial^4 \theta}{\partial s^4} + \left( \Lambda + \alpha K_b \left( \frac{\partial \theta}{\partial s} \right)^2 \right) \frac{\partial^2 \theta}{\partial s^2} \\ &\quad + \left( (\alpha + 1) \frac{\partial \Lambda}{\partial s} + \alpha F_p \right) \frac{\partial \theta}{\partial s} - u'(y) \alpha \zeta_f \sin^2(\theta). \end{aligned} \quad (29)$$

*Boundary conditions.* The flagellum boundary is free at  $s = L$  and the connection between the body and the flagellum is rigid. It gives the set of boundary conditions:

$$\frac{\partial \theta}{\partial s}(L, t) = \frac{\partial^2 \theta}{\partial s^2}(L, t) = \Lambda(L, t) = 0, \quad (30)$$

$$\theta(0, t) = \theta_0(t), \quad \Lambda(0, t) = \Lambda_0(t), \quad (31)$$

where  $\theta_0(t)$  and  $\Lambda_0(t)$  are respectively the angle of body with the  $x$ -axis and the tangential internal stress at the interface body/flagellum. We add the condition

$$N_0(t) = -K_b \frac{\partial^2 \theta}{\partial s^2}(0, t), \quad (32)$$

which is a consequence of the rigid connection between the body and the flagellum, combined with (23).

### Motion of the bacterial body

The motion of passive rigid ellipsoids is described by the Jeffery's equation. In the first order approximation, the flow around the ellipsoid can be treated as a planar shear flow. We describe the bacterial body motion by the Jeffery equations, where the shear rate is taken to be the flow rate at the center of the ellipsoid. We add an additional term corresponding to the normal internal stress coming from the flagellum. The modified Jeffery equation is written as

$$\begin{aligned} \frac{d\theta_0}{dt} &= -u'(y^h) \left( \frac{l^2}{l^2 + d^2} \sin^2 \theta_0(t) + \frac{d^2}{l^2 + d^2} \cos^2 \theta_0(t) \right) \\ &\quad + \frac{l}{2\zeta_\tau} N_0(t), \end{aligned} \quad (33)$$

where  $y^h$  is the  $y$ -coordinate of the center of mass of the ellipsoid. The velocity of the body center of mass has two components, the first comes from the flow, and the second comes from the stress of the flagellum. We neglect the perturbations produced by the body on the flow.

### Body-flagellum interface conditions

The body makes contact with the flagellum at  $s = 0$ . The rigidity of the junction enables the equality of the local velocities at the contact body/flagellum. Using (24), the local velocities of the flagellum are expressed as

$$\begin{aligned} v_\tau(0) &= u(y(0)) \cos \theta + \frac{1}{\zeta_f} \left[ \frac{\partial \Lambda}{\partial s}(0) + F_p - \kappa N_0 \right], \\ v_n(0) &= -u(y(0)) \sin \theta + \frac{1}{\zeta_f} \left[ \frac{\partial N}{\partial s}(0) + \kappa \Lambda_0 \right]. \end{aligned} \quad (34)$$

The velocities of the body are given by

$$\begin{aligned} v_\tau^h &= u(y^h) \cos \theta_0 + \frac{1}{\zeta_h} \Lambda_0 \\ v_n^h &= -u(y^h) \sin \theta_0 + \frac{1}{\zeta_h \alpha_h} N_0, \end{aligned} \quad (35)$$

where  $\zeta_h$  is the drag coefficient of the body,  $\zeta_h = 2\pi\eta_0 l / \log(l/d)$ , and  $\alpha_h$  is an anisotropy drag factor, taken to be 2 (slender body approximation, [40]). The tangential components of the velocities are the same, but there is an extra term for the normal velocities given that  $v_n(0)$  represents the normal velocity at the flagellum-body contact whereas  $v_{n,0}$  is the normal velocity of the center of the body which are at a distance  $\frac{l}{2}$  of each other.

$$v_\tau(0) = v_{\tau,0}, \quad v_n(0) = v_{n,0} + \frac{l}{2} \frac{d\theta_0}{dt}. \quad (36)$$

The equalities in (36) holding at  $s = 0$  are expressed as follows, using (34) and (35).

$$\begin{aligned} \frac{1}{\zeta_h} \Lambda_0 &= \cos(\theta_0) \left( u(y(0)) - u(y^h) \right) \\ &\quad + \frac{1}{\zeta_f} \left[ \frac{\partial \Lambda}{\partial s} + F_p + K_b \frac{\partial \theta}{\partial s} \frac{\partial^2 \theta}{\partial s^2} \right], \\ \frac{1}{\zeta_h \alpha_h} N_0 + \frac{l}{2} \frac{d\theta_0}{dt} &= -\sin(\theta_0) \left( u(y(0)) - u(y^h) \right) \\ &\quad + \frac{1}{\alpha \zeta_f} \left[ -K_b \frac{\partial^3 \theta}{\partial s^3} + \frac{\partial \theta}{\partial s} \Lambda \right]. \end{aligned} \quad (37)$$

### Expression of the coordinates

Since the swimmer's velocity depends on the local velocity of the ambient fluid, which itself depends on the  $y$ -coordinate, we express  $y^h(t)$  and  $y(s, t)$ , the vertical

position of the center body and of the flagellum respectively. We also study the evolution of the  $x$ -coordinate, as it is useful to describe the trajectories. Due to geometrical considerations, the body position  $(x^h, y^h)$  satisfies the following equations:

$$\begin{cases} \frac{dx^h(t)}{dt} = v_{\tau,0} \cos(\theta_0(t)) - v_{n,0}(t) \sin(\theta_0(t)), \\ \frac{dy^h(t)}{dt} = v_{\tau,0} \sin(\theta_0(t)) + v_{n,0} \cos(\theta_0(t)), \\ x^h(0) = x_0^h, \quad y^h(0) = y_0^h, \end{cases} \quad (38)$$

where  $(x_0^h, y_0^h)$  is the initial position of center of mass of the body. We substitute the expressions of the tangential and normal velocities (35) and obtain

$$\begin{cases} \frac{dx^h(t)}{dt} = u(x^h(t), y^h(t)) + \frac{1}{\zeta_h} \Lambda_0(t) \cos(\theta_0(t)) \\ \quad - \frac{1}{\alpha_h \zeta_h} N_0(t) \sin(\theta_0(t)), \\ \frac{dy^h(t)}{dt} = \frac{1}{\zeta_h} \Lambda_0(t) \sin(\theta_0(t)) + \frac{1}{\alpha_h \zeta_h} N_0(t) \cos(\theta_0(t)), \\ x^h(0) = x_0^h, \quad y^h(0) = y_0^h. \end{cases} \quad (39)$$

The positions of the flagellum may then be written in the form

$$\begin{cases} \frac{\partial x(s,t)}{\partial s} = \cos(\theta(s,t)) \\ \frac{\partial y(s,t)}{\partial s} = \sin(\theta(s,t)) \\ x(0,t) = x^h(t) + \frac{l}{2} \cos(\theta_0(t)), \\ y(0,t) = y^h(t) + \frac{l}{2} \sin(\theta_0(t)). \end{cases} \quad (40)$$

## Rescaling

We first define the order of magnitude of the shear rate as  $\gamma_0$ . The variables are rescaled as

$$\begin{aligned} \tilde{s} &= \frac{s}{L}, \quad \tilde{u} = \frac{u}{L\gamma_0}, \quad \tilde{t} = \gamma_0 t, \quad \tilde{\Lambda} = \frac{\Lambda}{\zeta_f \gamma_0 L^2}, \\ \tilde{\Lambda}_0 &= \frac{\Lambda_0}{\zeta_f \gamma_0 L^2}, \quad \tilde{N}_0 = \frac{N_0}{\zeta_f \gamma_0 L^2}, \quad \zeta_r = \frac{l^2 \zeta_h}{6}, \\ \tilde{K}_b &= \frac{K_b}{\zeta_f \gamma_0 L^4}, \quad \tilde{F}_p = \frac{F_p}{\zeta_f \gamma_0 L}, \quad k_r = \frac{L \zeta_f}{\zeta_h}, \\ \beta &= \frac{d^2}{l^2 + d^2}, \end{aligned}$$

In Section 2, we use these rescaled variables but we omit the tildes, to simplify the notation.

## 6.2 Random reorientation (tumbling)

We define  $T_{run}$  as the time between two random reorientation. If we denote by  $N_t$  the number of reorientations occurring before time  $t$ , we have

$$\mathbb{P}[(N_t - N_s) = k] = e^{-\lambda_r(t-s)} \frac{(\lambda_r(t-s))^k}{k!}, \quad (41)$$

where  $\mathbb{P}$  is probability of the event. This causes the distribution of run duration to be exponential. Indeed, if  $T_{run1}$  is the time at which first reorientation occurs, we have

$$\mathbb{P}(T_{run1} \geq t) = \mathbb{P}(N_t = 0) = \exp(-\lambda_r t), \quad (42)$$

which means that the time of the first run has an exponential distribution. The parameter  $\frac{1}{\lambda_r}$  is the expectation of  $T_{run}$  and is taken to be 10 min.

To simulate the exponential distribution, we generate a uniform random variable  $U$  using a random number generator in **C++**. We denote by  $G$  the inverse of the repartition function of the exponential law, namely  $G(u) = -\frac{1}{\lambda_r} \ln(1-u)$ , then the random variable  $G \circ U$  has an exponential distribution, since

$$\mathbb{P}(G \circ U \leq t) = \mathbb{P}(U \leq F(t)) = F(t). \quad (43)$$

### 6.2.1 Effects of the nonlinear flow profile

In the analysis above we neglected the effect due to the nonlinear profile of the flow. In the context of a spherical particle in an unbounded flow, the lift force exerted by the fluid on a body whose center is in  $y^h$  is of the form

$$\text{Lift} = 6.46 \eta_0 r \Delta u \frac{\sqrt{R}}{4}, \quad R = \rho u'(y^h) \frac{r^2}{\eta_0}, \quad (44)$$

where  $\rho$  is the ratio between the solid and the fluid density,  $\Delta u$  is the slip velocity of the particle (the particle velocity minus the undisturbed velocity at the particle center), and  $r$  is the radius of the body (see [42, 43]). This expression is valid only for spherical swimmers. In our case, the swimmer is close to a rod of length  $l$ . Thus, in (44) we replace the radius  $r$  by the effective radius,  $\frac{l}{2} |\sin(\theta_0)|$ , which corresponds to the radius seen by the fluid. This results in  $\Delta u = |u(y^h + \frac{l}{2} \sin(\theta_0)) - u(y^h)| \approx |4l \sin(\theta_0)|$ .

In the Poiseuille flow, assuming that  $\rho = 1$ , the formula becomes

$$\text{Lift} = \frac{6.46}{4} \sqrt{\eta_0} \sqrt{u'(y^h)} p l^3 |\sin^3(\theta_0)| \mathbf{y} \mathbf{e}_y, \quad (45)$$

With the order of magnitude of the parameters,  $\text{Lift} \approx 10^{-14} N$ , which can be neglected, in comparison to the total propulsion force  $L \times F_p$ , which is of the order of few pN. The model including this lift effect was implemented, and no noticeable change in the behavior was observed.

Parameter	Parameter value
$\alpha$	2
$\beta$	0.0192
$\gamma$	0.1 1/s
$d$	$7 \cdot 10^{-7}$ m
$\eta_0$	$10^{-3}$ Pa.s
$F_p$	$10^{-7}$ N/m
$K_b$	$3 \cdot 10^{-23}$ N.m <sup>2</sup>
$L$	$10^{-5}$ m
$l$	$5 \cdot 10^{-6}$ m
$\zeta_f$	$10^{-3}$ N.s/m <sup>2</sup>
$\zeta_h$	$2 \cdot 10^{-8}$ N.s/m
$p$	$10^4$ 1/(m s)
$w$	$4 \cdot 10^{-4}$ m

Table 1: Parameter values used in the numerical simulations

Rescaled variable	Representative value
$b$	$5 \cdot 10^{-3}$
$c$	-0.0045
$F_p$	100
$K_b$	30
$k_r$	0.5
$E$	1

Table 2: Numerical values of the rescaled variables

## Glossary

$\alpha$	Drag anisotropy factor
$\beta$	Bretherton constant of the ellipsoidal body
$\gamma$	Shear rate
$d$	Thickness of the body
$\eta_0$	Viscosity of the surrounding fluid
$F_p$	Propulsion force density
$K_b$	Bending stiffness
$k_r$	Non-dimensional parameter
$\Lambda$	Internal stress of the flagellum (tangential part)
$\lambda_r$	Parameter of the Poisson process
$L$	Length of the flagellum
$l$	Length of the body
$N$	Internal stress of the flagellum (normal part)
$p$	Pressure gradient of the Poiseuille flow
$s$	Current coordinate on the flagellum
$t$	Time
$\theta_0$	Body angle (swimmer orientation)
$\theta$	Angle of the flagellum
$(\boldsymbol{\tau}, \mathbf{n}, \mathbf{b})$	Frenet system
$u$	Fluid velocity
$(v_\tau, v_n)$	Flagellum velocity in Frenet coordinates
$(v_{\tau,0}, v_{n,0})$	Body velocity in Frenet coordinates
$w$	Radius of the channel
$(x^h, y^h)$	Coordinate of the body center
$\zeta_f$	Friction coefficient for the flagellum
$\zeta_h$	Friction coefficient for the head

## References

- [1] R. Stocker, Marine Microbes See a Sea of Gradients. *Science* **338**, 628-633, 2012.
- [2] M. T Butler, Q. Wang, and R. M. Harshey, Cell Density and Mobility Protect Swarming Bacteria Against Antibiotics. *PNAS* **107**, 3776, 2010.
- [3] C. Dombrowski, L. Cisneros, S. Chatkaew, R. E. Goldstein, and J. O. Kessler, Self-Concentration and Large-Scale Coherence in Bacterial Dynamics. *Phys. Rev. Lett.* **93**, 098103, 2004.
- [4] A. Sokolov, I.S. Aranson, J.O. Kessler, and R.E. Goldstein, Concentration dependence of the collective dynamics of swimming bacteria. *Phys. Rev. Lett.* **98**, 158102, 2007.
- [5] A. Sokolov and I. S. Aranson, Physical Properties of Collective Motion in Suspensions of Bacteria. *Phys. Rev. Lett.* **109**, 248109, 2012.
- [6] J. Dunkel, S. Heidenreich, K. Drescher, H. H. Wensink, M. Br, and R. E. Goldstein, Fluid Dynamics of Bacterial Turbulence. *Phys. Rev. Lett.* **110**, 228102, 2013.
- [7] S. D. Ryan, B. M. Haines, L. Berlyand, F. Ziebert, and I. S. Aranson, Viscosity of bacterial suspensions: Hydrodynamic interactions and self-induced noise. *Phys. Rev. E* **83**, 050904, 2011.
- [8] D. Saintillan and M. Shelley, Instabilities and Pattern Formation in Active Particle Suspensions: Kinetic Theory and Continuum Simulations. *Phys. Rev. Lett.* **100**, 178103, 2008.
- [9] I. S. Aranson, A. Sokolov, J. O. Kessler, and R. E. Goldstein, Model for Dynamical Coherence in Thin Films of Self-Propelled Microorganisms. *Phys. Rev. E* **75**, 040901, 2007.
- [10] H. H. Wensink, J. Dunkel, S. Heidenreich, K. Drescher, R. E. Goldstein, H. Lwen, and J. M. Yeomans, Meso-scale Turbulence in Living Fluids. *PNAS* **109**, 14308, 2012.
- [11] S. D. Ryan, A. Sokolov, L. Berlyand, and I. S. Aranson, Correlation properties of collective motion in bacterial suspensions. *New J. Phys.* **15**, 105021, 2013.
- [12] L. H. Cisneros, J. O. Kessler, S. Ganguly, and R. E. Goldstein. Dynamics of swimming bacteria: Transition to directional order at high concentration. *Phys. Rev. E* **83**, 061907, 2011.
- [13] J. Adler. Chemotaxis in bacteria. *Science* **153**, 708-716, 1966.
- [14] R. Vogel and H. Stark. Motor-driven bacterial flagella and buckling instabilities. *Eur. Phys. J. E* **35**, 1-15, 2012.
- [15] R. Vogel and H. Stark. Rotation-induced polymorphic transitions in bacterial flagella. *Phys. Rev. Lett.* **110**, 158104, 2013.

- [16] K. Son, J. S. Guasto, and R. Stocker. Bacteria can exploit a flagellar buckling instability to change direction. *Nature Phys.* **9**, 494-498, 2013.
- [17] F. P. Bretherton and L. Rotshchild. Rheotaxis of spermatozoa. *Proc. R. Soc. Lond. B. Biol. Sci.* **153**, 490-502, 1961.
- [18] K. Miki and D.E. Clapham, Rheotaxis guides mammalian sperm. *Curr Biol.* **23**, 443-52, 2013.
- [19] V. Kantsler, J. Dunkel, M. Blayney, R. E. Goldstein. Rheotaxis facilitates upstream navigation of mammalian sperm cells. *eLife* **3**, e02403, 2014.
- [20] P. Denissenko, V. Kantsler, D. J. Smith, and J. Kirkman-Brown. Human spermatozoa migration in microchannels reveals boundary-following navigation. *PNAS* **109**, 8007-8010, 2012.
- [21] V. Kantsler, J. Dunkel, M. Polin, and R. E. Goldstein. Ciliary contact interactions dominate surface scattering of swimming eukaryotes. *PNAS* **110**, 11871192, 2012.
- [22] A. Zöttl and H. Stark. Non linear dynamics of a Microswimmer in Poiseuille flow. *Phys. Rev. Lett.* **108**, 21804, 2012.
- [23] A. Zöttl and H. Stark. Periodic and quasiperiodic motion of an elongated microswimmer in Poiseuille flow. *Eur. Phys. J. E* **36**, 1-10, 2012.
- [24] S. Chilukuri, C. H. Collins and P. T. Underhill. Impact of external flow on the dynamics of swimming microorganisms near surfaces. *J. Phys. Condens. Matter.* **26**, 115101, 2014.
- [25] A. P. Berke, L. Turner, H. C. Berg and E. Lauga, Hydrodynamic Attraction of Swimming Microorganisms by Surfaces. *Phys. Rev. Lett.* **101**, 038102, 2008.
- [26] K. Drescher, J. Dunkel, L. H. Cisneros, S. Ganguly, and R. E. Goldstein, Fluid dynamics and noise in bacterial cell-cell and cell-surface scattering. *PNAS* **108**, 10940-10945, 2011.
- [27] R. Rusconi, J. S. Guasto and R. Stocker. Bacterial transport suppressed by fluid shear. *Nature physics* **10**, 212-217, 2014.
- [28] G. I. Taylor. The action of waving cylindrical tails in propelling microscopic organisms. *Proc. R. Soc. Lond.* **221**, A211-225, 1952.
- [29] E. M. Purcell. The efficiency of propulsion by a rotating flagellum. *PNAS* **94**, 11307-11311, 1997.
- [30] S. Jung, K. Mareck, L. Fauci and J. M. Shelley. Rotational dynamics of a superhelix towed in a Stokes fluid. *Physics of Fluids* **19**, 103-105, 2007.
- [31] Marcos, H. C. Fu, T. R. Powers, and R. Stocker. Bacterial rheotaxis. *PNAS* **109**, 4780-4785, 2012.
- [32] J. O. Kessler. Hydrodynamic focusing of motile algal cell. *Nature* **313**, 218-220, 1985.
- [33] L. Karp-Boss, L.E. Boss, and P. A. Jumars. Motion of dinoflagellates in a simple shear flow. *Limnol. Oceanogr.* **45**, 15961602, 2000.
- [34] G. B. Jeffery. The motion of ellipsoidal particles in a viscous fluid. *Proc. R. Soc. Lond.* **179**, 102-161, 1922.
- [35] W.R. DiLuzio, L. Turner, M. Mayer, P. Garstecki, D.B. Weibel, H.C. Berg, and G. W. Whitesides. Escherichia coli swim on the right-hand side. *Nature*, **435**, 1271-1274, 2005.
- [36] A. Sokolov, I.S. Aranson, Reduction of viscosity in suspension of swimming bacteria. *Phys. Rev. Lett.* **103**, 148101, 2009.
- [37] J. Gachelin, G. Miño, H. Berthet, A. Lindner, A. Rousselet, and E. Clément, Non-Newtonian Viscosity of Escherichia coli Suspensions. *Phys. Rev. Lett.* **110**, 268103, 2013.
- [38] B.M. Haines, A. Sokolov, I.S. Aranson, L. Berlyand, D.A. Karpeev, Three-dimensional model for the effective viscosity of bacterial suspensions. *Phys. Rev. E* **80**, 041922, 2009.
- [39] G. K. Batchelor. Slender-body theory for particles of arbitrary cross-section in Stokes flow. *J. Fluid Mech.* **44**, 419-440, 1970.
- [40] M. Roper, R. Dreyfus, J. Baudry, M. Fermigie, J. Bibette, and H.A. Stone. On the dynamics of magnetically driven elastic filaments. *J. Fluid Mech.* **554**, 167-190, 2006.
- [41] H. C. Berg. E. coli in motion. *Springer-Verlag*, 2004.
- [42] G. Segré and A. Silverberg. Behaviour of macroscopic rigid spheres in Poiseuille flow. *J. Fluid Mech.* **14**, 136-157, 1962.
- [43] P. G. Saffman. The lift on a small sphere in a slow shear flowing. *J. Fluid Mech.* **22**, 385-400, 1965.